DRAFT VERSION AUGUST 22, 2023
Typeset using LaTeX **twocolumn** style in AASTeX63

Magnetic Reconnection as the Key Mechanism in Sunspot Rotation Leading to Solar Eruption

CHAOWEI JIANG,[1,2] XUESHANG FENG,[1,2] XINKAI BIAN,[1] PENG ZOU,[1] AIYING DUAN,[3] XIAOLI YAN,[4] QIANG HU,[5] WEN HE,[5] XINYI WANG,[2] PINGBING ZUO,[1,2] AND YI WANG[1,2]

[1]*Shenzhen Key Laboratory of Numerical Prediction for Space Storm, Institute of Space Science and Applied Technology, Harbin Institute of Technology, Shenzhen 518055, China*

[2]*Key Laboratory of Solar Activity and Space Weather, National Space Science Center, Chinese Academy of Sciences, Beijing 100190, China*

[3]*School of Atmospheric Sciences, Sun Yat-sen University, Zhuhai 519000, China*

[4]*Yunnan Observatories, Chinese Academy of Sciences, Kunming 650216, China*

[5]*Center for Space Plasma and Aeronomic Research, The University of Alabama in Huntsville, Huntsville, AL 35899, USA*

Submitted to *ApJ*

ABSTRACT

The rotation of sunspots around their umbral center has long been considered as an important process in leading to solar eruptions, but the underlying mechanism remains unclear. A prevailing physical picture on how sunspot rotation leads to eruption is that, by twisting the coronal magnetic field lines from their footpoints, the rotation can build up a magnetic flux rope and drive it into some kinds of ideal magnetohydrodynamics (MHD) instabilities which initiate eruptions. Here with a data-inspired MHD simulation we studied the rotation of a large sunspot in solar active region NOAA 12158 leading to a major eruption, and found that it is distinct from prevailing theories based on ideal instabilities of twisted flux rope. The simulation suggests that, through successive rotation of the sunspot, the coronal magnetic field is sheared with a central current sheet created progressively within the sheared arcade before the eruption, but without forming a flux rope. Then the eruption is instantly triggered once fast reconnection sets in at the current sheet, while a highly twisted flux rope is created during the eruption. Furthermore, the simulation reveals an intermediate evolution stage between the quasi-static energy-storage phase and the impulsive eruption-acceleration phase. This stage may corresponds to slow-rise phase in observation and it enhances building up of the current sheet.

Keywords: Sun: Magnetic fields; Sun: Flares; Sun: corona; Sun: Coronal mass ejections

1. INTRODUCTION

Magnetic fields play a defining role for solar activities, especially, solar eruptions such as solar flares and coronal mass ejections (CMEs). The most visible manifestation of solar magnetic field are sunspots as seen on the solar surface (namely, the photosphere), which represent regions where the strongest magnetic field protrudes from the solar interior into the atmosphere. When rotating along with the solar surface, sunspots are also commonly observed to be rotating around their umbral center (Brown et al. 2003; Zhang et al. 2007; Yan et al. 2008; Min & Chae 2009; James et al. 2020), which has been discovered a century ago (Evershed. 1910; St. John 1913). Such rotational motion of sunspots has long been considered as an important process in association with generation of solar eruptions, because it is an efficient mechanism for transporting free magnetic energy and helicity from below the photosphere into the corona (Stenflo 1969; Barnes & Sturrock 1972). Indeed, almost all the flare-productive solar active regions (ARs) have been reported with significant sunspot rotations (Yan et al. 2008), for example, in the extensively studied ARs including NOAA 10930 (Min & Chae 2009; Zhang et al. 2007), 11158 (Jiang et al. 2012; Vemareddy et al. 2012), 11429 (Zheng et al. 2017), 12158 (Bi et al. 2016; Vemareddy et al. 2016), and 12673 (Yan et al. 2018b,a), etc.

A widely-believed physical picture on how sunspot rotation leads to eruption is that, by twisting the coronal magnetic field lines at their footpoints, the rotation can build up a magnetic flux rope (MFR, which is a bundle of magnetic flux possessing a significant amount of twist, typically characterized by a field-line twist number above unity (Chen 2017; Cheng et al. 2017; Liu 2020)), and drive it into some kinds of ideal magnetohydrodynamics (MHD) instabilities (for example, the kink instability and torus instability, Kliem & Török 2006; Török & Kliem 2005; Fan & Gibson 2007; Aulanier et al. 2010) or catastrophic loss of equilibrium (Forbes & Isenberg 1991; Lin & Forbes 2000; Kliem et al. 2014). For example, in the comprehensive review book "New Millen-

nium Solar Physics" (Aschwanden 2019), a section is devoted to the studies of rotating sunspots and it is written that "The relationship between rotating sunspots and the triggering of a flare accompanied by a sigmoid eruption, most likely driven by a kink instability, is overwhelming."

It seems evident that the rotational motion of magnetic field line footpoints (around the rotating center) can increase magnetic twist degree of the flux rope (around the rope axis that roots at the rotating center), until it reaches a critical value for kink instability (Hood & Priest 1979; Mikic et al. 1990; Galsgaard & Nordlund 1997). Or, the flux rope will expand upward owing to the increase of magnetic pressure as driven by the rotation (Aulanier et al. 2005), and reaches a critical height at which the torus instability (Kliem & Török 2006) (or equivalently, the catastrophic loss of equilibrium (Kliem et al. 2014)) sets in. However, none of these scenarios has been proven in MHD simulations that start from a magnetic arcade and are driven by solely line-tied surface rotation motion without other requirements (for example, flux cancellation (Amari et al. 2003; Aulanier et al. 2010)). For example, all previous attempts of such type of simulations (Amari et al. 1996; Török & Kliem 2003; Aulanier et al. 2005) show that the continuous twisting of the core field in a bipolar potential field can lead to a strong expansion (or "fast opening") of the field, but such expansion cannot be taken as solar eruption since there is no impulsive release (increase) of magnetic (kinetic) energy, and the expansion process can always relax smoothly to an equilibrium if the driving velocities are suppressed, therefore not associated with an instability or a loss of equilibrium (Aulanier et al. 2005). There is only one simulation (Török et al. 2013) designed to show that sunspot rotation can cause the arcade overlying a pre-existing flux rope to inflate, thus weakening the confining effect on the flux rope and letting it to ascend slowly until reaching the torus instability. But such a simulation does not show how the flux rope forms, and moreover the rotating sunspot does not energize the key structure of eruption (i.e., the flux rope, which is not rooted in the rotating sunspot in their simulation), therefore not playing a direct role in triggering the eruption.

In this paper, we carried out a data-inspired MHD simulation based on observational rotation for solar AR NOAA 12158 which contains a prominent rotating sunspot that eventually produced a X-class eruptive flare. Our simulation follows the long-term evolution of the AR until the eruption, and it is shown that the mechanism of the sunspot rotation leading to eruption is different from the aforementioned ones. Our simulation shows that by applying surface rotation flow to the major sunspot, the nonpotentiality of the coronal magnetic field, as measured by the ratio of the total magnetic energy to the corresponding potential field energy, increases monotonically while the kinetic energy keeps a small value, as the MHD system evolves quasi-statically. At a critical time, there is a clear transition from the quasi-static state to an eruptive phase in which the kinetic energy impulsively rises and the magnetic energy releases quickly. Such a key transition is associated with a vertical current sheet created progressively in the sheared arcade as driven by the sunspot rotation. Once tether-cutting reconnection (Moore et al. 2001) sets in at the current sheet, the eruption is inevitably triggered even when we turn off the boundary driving, and a highly twisted flux rope originates from the eruption, forming a CME. This confirms the fundamental mechanism of solar eruption initiation as recently established for an idealized bipolar magnetic configuration (Jiang et al. 2021c; Bian et al. 2022a,b), in which a current sheet is formed by quasi-statically shearing the bipolar arcade until reconnection at the current sheet triggers an eruption. Moreover, our simulation revealed a slow-rise evolution phase connecting the quasi-static energy-storage phase and the impulsive eruption-acceleration phase, and it plays an important role in enhancing the building up of the current sheet. In the following, we first give an observational analysis of the studied event in Section 2, then describe our numerical modeling settings in Section 3 and show the simulation results in Section 4, and finally conclude and give discussions in Section 5.

2. OBSERVATIONS

2.1. *Overview of the event*

When first appearing on the solar disk on 5 September 2014, AR NOAA 12158 was already in its decaying phase, while its leading sunspot witnessed with continuous counterclockwise rotation from 6–11 September 2014 during its passage on the solar disk (Figure 1). As dominated by the sunspot rotation, the coronal configuration of the AR is driven to form an inverse S-shaped structure with hot emission as seen in the 94 Å image (Figure 1b) of Atmospheric Imaging Assembly (AIA) onboard Solar Dynamics Observatory (SDO), i.e., a sigmoid, surrounded by cooler large-scale loops as seen in AIA 171 Å (Figure 1a). At around 17:00 UT on 10 September, the AR produced a Geostationary-Operational-Environmental-Satellite (GOES) X1.6 flare, which was accompanied with a global eruption of the AR resulting in a halo CME (Vemareddy et al. 2016), and our simulation aims to follow the coronal magnetic evolution from 00:00 UT on 8 September 2014 until this major eruption.

2.2. *Observation of the eruption*

Figure 2 (and its animation) shows the eruption process imaged in three AIA channels. With about 20 min before the flare onset, a precursor is observed; in the hot channel of AIA 131 Å, a few loops in the core of the sigmoid became more and more prominent, while the transverse width of this brightening structure became progressively thinner,

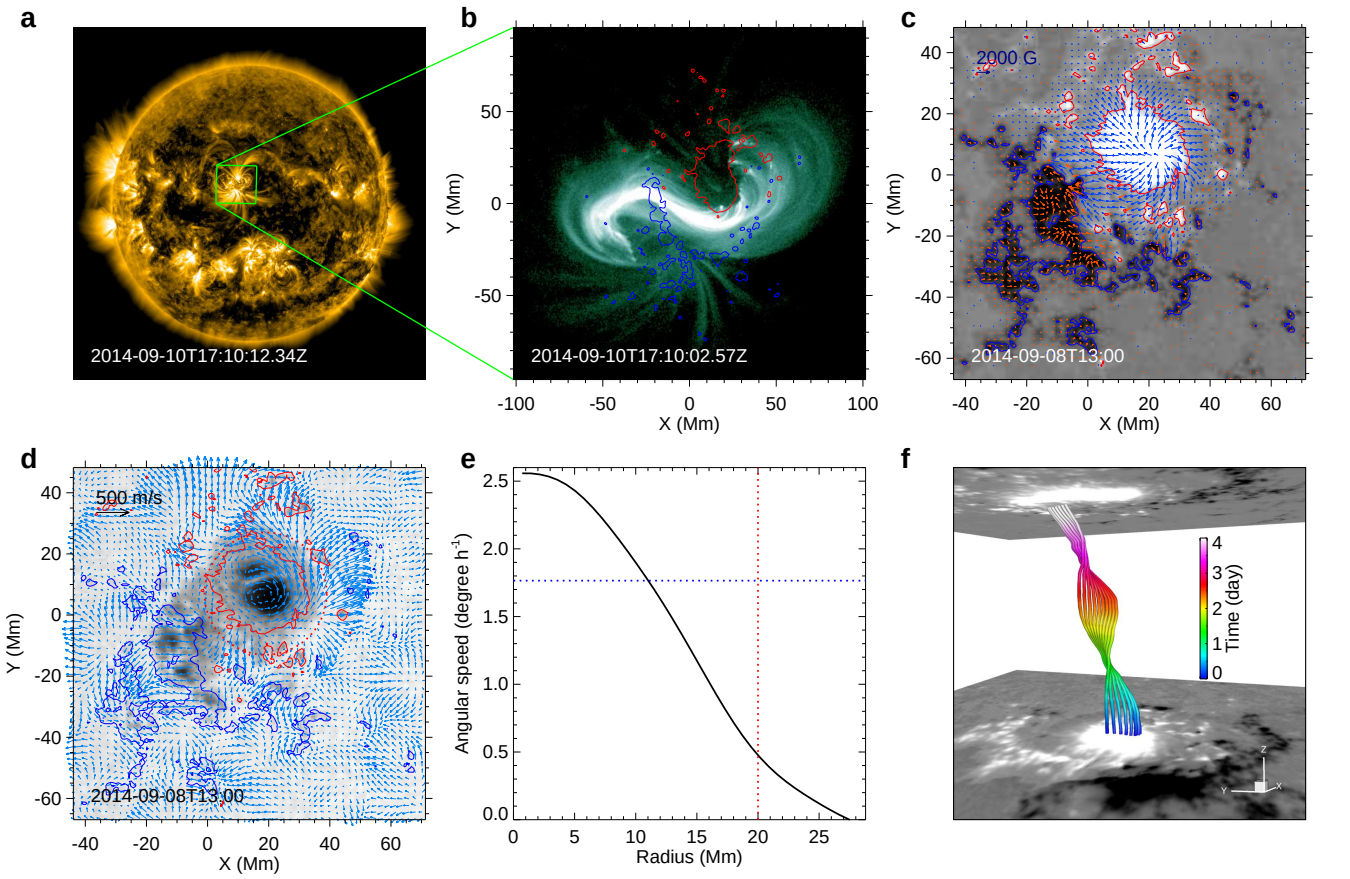

Figure 1. Observation of coronal structure and the rotational sunspot in AR 12158. a, Full-disk image of the Sun taken by SDO/AIA in 171 Å channel at 10 min before onset of the X1.6 flare. The boxed region denotes the location of the target AR. **b**, The enlarged view of the AR in SDO/AIA 94 Å channel which presents a coronal sigmoid with reverse S shape. The colored curves are shown for the contour lines of the vertical magnetic field B_z, with red (blue) representing $B_z = 500$ (-500) G. **c**, Vector magnetogram observed by SDO/HMI at two days before the flare. The arrows show the horizontal field components with blue (red) in region of $B_z > 0$ (< 0). **d**, Surface velocity field (the vectors colored in green) overlaid on the SDO/HMI continuum image of the AR. The main sunspot is denoted by the circle with a radius of 20 Mm. **e**, Profile of the angular speed at different radial distance from the rotation center. Here the angular speed is averaged for three days of 8–10 September 2014. The red line denotes the edge of the sunspot at 20 Mm, and the blue line denotes the angular speed of 1.75° h^{-1}, which is averaged value within the radial distance of 0 to 20 Mm and thus approximates the rotation rate of the sunspot as a whole. **f**, 3D shape of the trajectories of the surface flow with the z axis representing time direction, and the color also denotes time. The bottom and top surfaces represent the magnetogram observed at 00:00 UT on 7 and 00:00 UT on 11 of September 2014, respectively.

which possibly hints that a pre-flare current sheet was forming gradually there. Meanwhile, a set of coronal loops, likely overlying the middle part of the sigmoid, expanded outward slowly, which looks rather faint but still detectable in different AIA channels and can be clearly seen in the base difference images of AIA 193 Å (Figure 2c). The speed in the direction from the flare core to the southwest is estimated to be around 10 km s^{-1} (Figure 3), which is at least an order of magnitude larger than a quasi-static evolutionary speed that is driven by the photospheric motions (note that the actual expansion speed of these loops is underestimated due to the projection effect). At 17:21 UT, the soft X-ray flux increased impulsively (Figure 3a), which indicates the onset of fast reconnection. Instantly, the slow-expanding loops were accelerated impulsively within about 3 min, reaching a speed of $\sim$ 800 km s^{-1} at 17:26 UT (Figure 3b and c). The peak value of acceleration reaches above $\sim$ 10 km s^{-2}, which is on the same order of magnitude of acceleration as observed in the most impulsive eruption events. Such strong acceleration is not likely driven by an ideal MHD instability of MFR, according to a study by Vršnak (2008), who used a analytic model of flux rope to study the acceleration of eruption as driven by ideal evolution and resistive evolution. They concluded that "The purely ideal MHD process cannot account for highest observed accelerations which can attain values up to 10 km s^{-2}. Such accelerations can be achieved if the process of reconnection beneath the erupting flux-rope is included into the model." (see also Green et al. 2018).

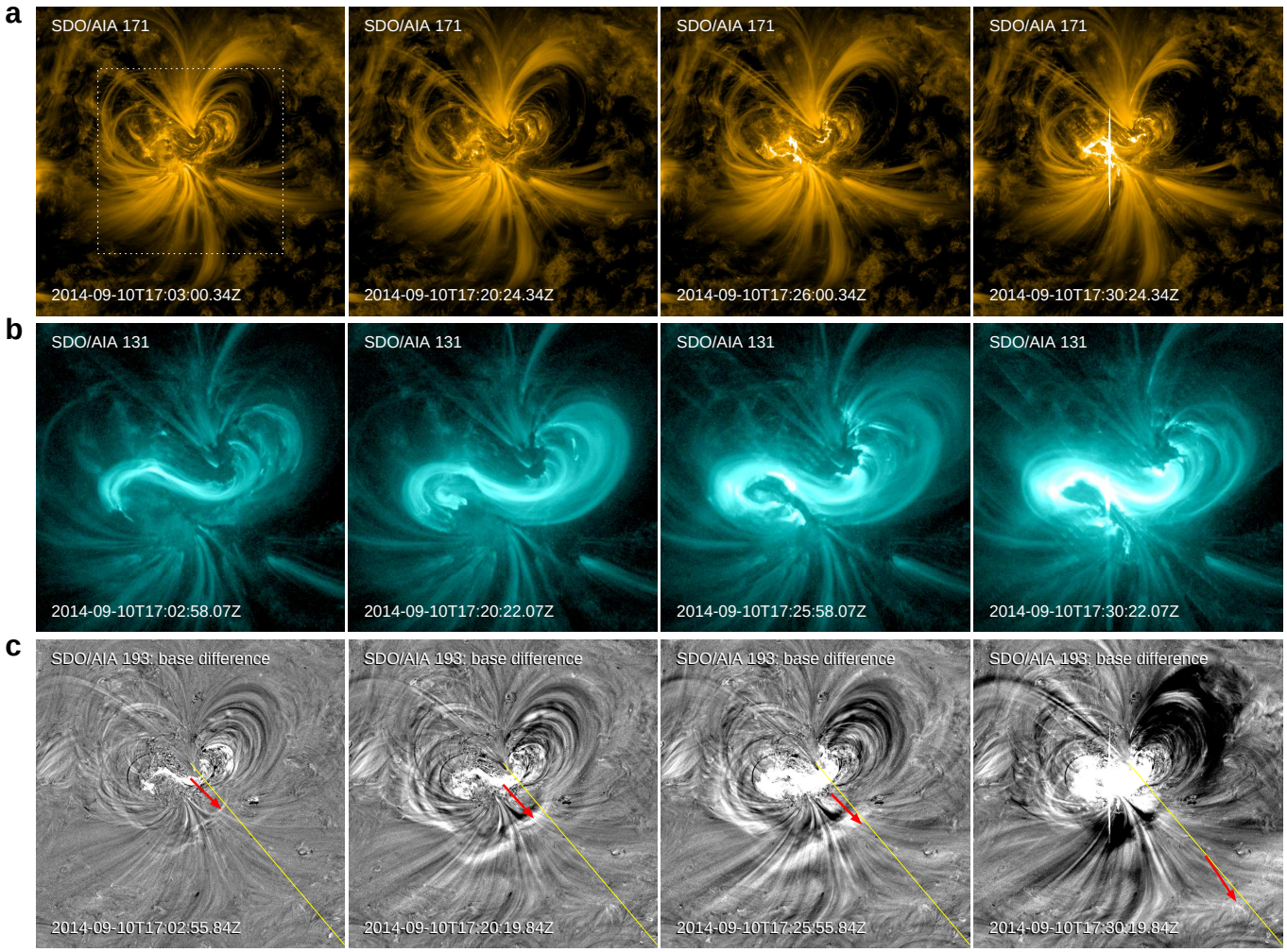

Figure 2. EUV imaging of the X1.6 flare taken by SDO/AIA. a, Images in 171 Å channel. **b**, 131 Å channel, with a smaller field of view (as denoted by the dashed box in **a**) to show the core region of the flare site. **c**, Base difference images of the 193 Å channel. The yellow line denotes the slit for which the time-distance map in Figure 3b is shown. The red arrows show the moving of an erupting loop-like structure that experienced first a slow rise well before (for around 20 min) the flare onset time and then an impulsive acceleration in the first few minutes during the flare, with more details shown in Figure 3. The animation attached shows the flare eruption observed by SDO/AIA in different EUV wavelengths and the associated soft X-ray light curve recorded by GOES. In particular, the first two top panels and the bottom middle panel correspond to the three panels in this figure, respectively. The top right panel shows soft X-ray light curve. The bottom left panel shows the AIA observation in 193 Å. The bottom right panel shows the time-distance stack plot for the slit as shown in the bottom middle panel.

With start of the impulsive phase of the flare, the flare ribbons and post-flare loops were seen with slipping-like motions, which are interpreted to be a manifestation of 3D slipping reconnection that forms an MFR during flare (Li & Zhang 2015; Dudík et al. 2016; Gou et al. 2023), and a twin set of coronal dimmings were observed in both AIA 171 and 193 Å channels along with the eruption, which should map the feet of the erupting MFR. Although some lowing-lying filaments were observed at the flare site (Dudík et al. 2016), they did not erupt with the flare. Previous studies of the same event using coronal nonlinear force-free field extrapolation also suggest that only a sheared arcade rather than a well-defined MFR existed prior to this eruption (Duan et al. 2017; Shen et al. 2022).

2.3. *Estimation of sunspot rotation*

To guide the simulation, we first estimate the degree of the sunspot rotation in the three days of 8–10 September 2014. To estimate the degree of its rotation with respect to the sunspot center, we calculate the surface velocity at the photosphere based on a time sequence of vector magnetograms, and further extract the velocity components that are directly associated with the rotational motion from the surface flow. Then, by integration of the rotational speed with time, it provides an alternative way of estimation the rotational degree to the traditional method based on direct inspection of the white-light continuum images (Brown & Walker 2021; Vemareddy et al. 2016). The surface velocity at the photosphere is derived using a velocity-recovering method

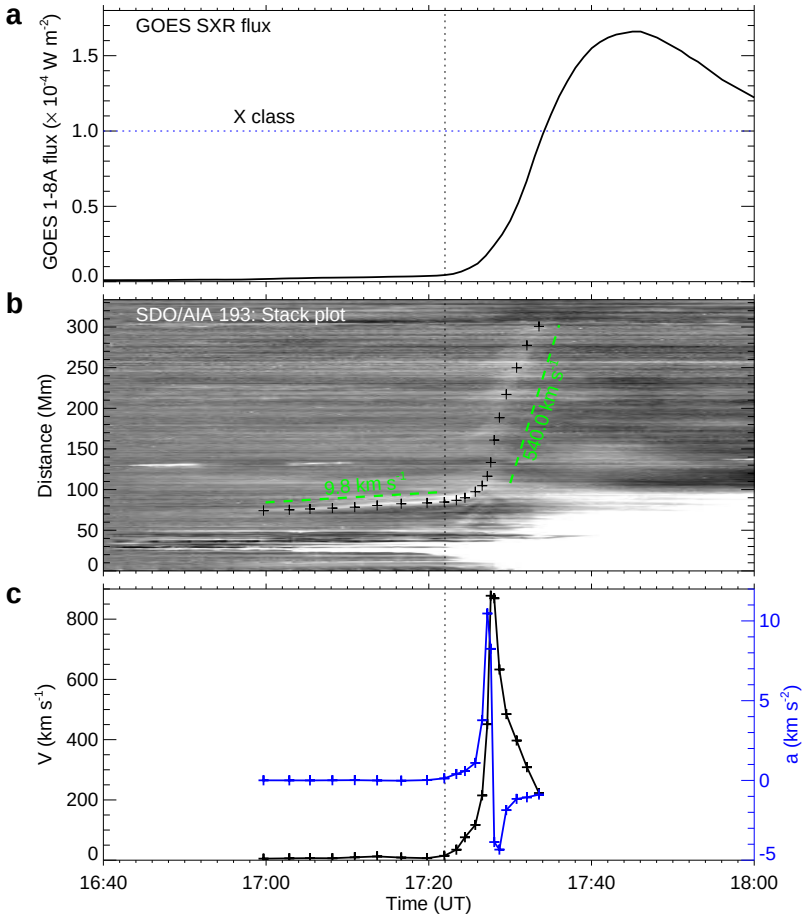

Figure 3. Slow rise and impulsive acceleration of the erupting coronal loops. a, GOES soft X-ray flux observed in the time period around the X1.6 flare. The vertical dashed line denotes the start of the fast rise of the flux. The horizontal dashed line denotes the level of flux that is defined for flare reaching X class. **b**, Time-distance stack plot for the slit as shown in Figure 2c. The plus signs overlaid are sampled to get the data of time and distance of the erupting loop-like structure, which shows first a slow rise and then an impulsive acceleration. The average speeds of the slow rise phase and the eruption phase are denoted by the green dashed lines. **c**, Evaluation of velocity and acceleration of the erupting structure as shown in **b** based on the sampled data points.

called DAVE4VM (Schuck 2008). It is a differential affine velocity estimator (DAVE) designed for vector magnetogram (VM), which uses a variational principle to minimize statistically deviations in the magnitude from the magnetic induction equation. The vector magnetograms are provided by the SDO Helioseismic and Magnetic Imager (HMI) SHARP data with cadence of 12 minutes and pixel size of 1 arcsec (by rebinning the original data with pixel size of 0.5 arcsec). Since there are a few time gaps[1] in our studied time interval, we first filled the data gap using linear interpolation in the time domain to generate a complete time series from 00:00 UT on 8 September 2014 to 24:00 UT on 10 September 2014. Then we input the time series of vector magnetogram into the DAVE4VM code. We set the window size of sampling, a key parameter in the DAVE4VM code, as its optimized value of 19 pixels or 9.5 arcsec (Liu & Schuck 2012; Liu et al. 2014).

After obtaining the surface velocity, we made a correction by removing the velocity component parallel to the magnetic field, since this field-aligned velocity is artificial and makes no contribution in the magnetic induction equation Schuck (2008). To reduce the data noises, the time series of flow maps are smoothed in both the time and space domains, with a Gaussian FWHM of 2 hours for time (i.e., 10 times of the data cadence) and 6 arcsec for both x and y directions, respectively. Figure 1d shows a snapshot of the surface velocity after this smoothing. The speed of the flow is generally a few hundreds of meters per second and the main feature is a clear and persistent rotation of the main sunspot. Note that during the three days the basic configuration of the photospheric magnetic flux distribution is rather similar with only gradual dispersion as small magnetic flux fragments, known

[1] Specifically, 4 time gaps of around 2 hours which are, respectively, 06:12 UT to 08:48 UT on 8 September, 06:00 UT to 08:48 UT on 9 September, 00:12 UT to 03:00 UT and 06:00 UT to 08:48 UT on 10 September.

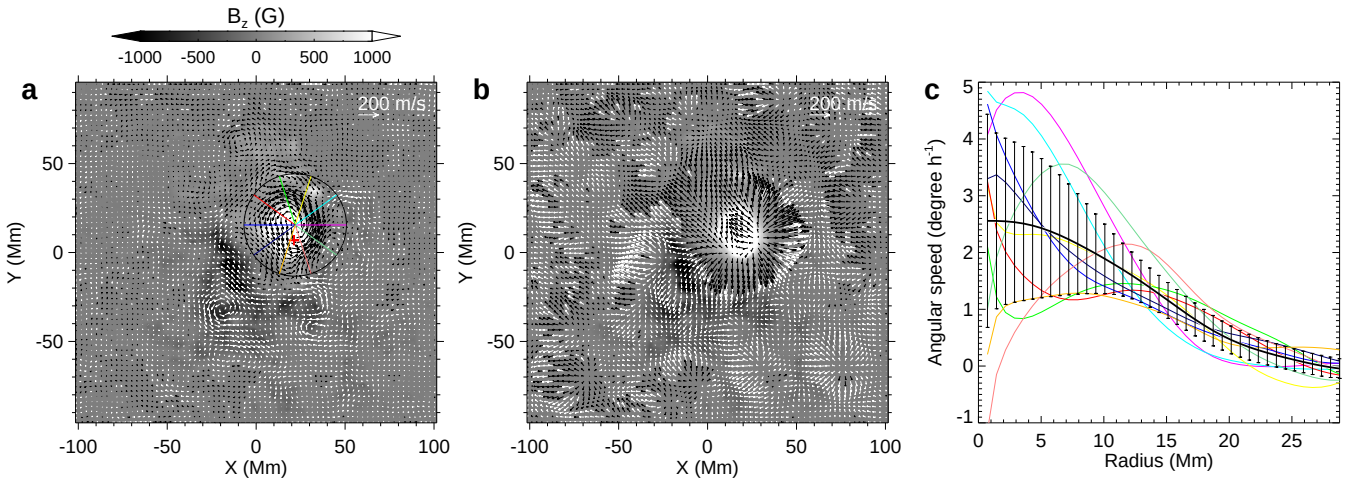

Figure 4. Estimation of the rotation speed of the sunspot. a, Vectors show the divergence-free component $\mathbf{v}_1$ of the surface flow averaged for the three-day data covering 2014 September 8-10. The background image shows the magnetic flux density B_z, also averaged for the three-day HMI data. The circle denotes the rotating sunspot, and the centre of the circle is the rotating center. The radial lines are sampled to estimate the profile of angular speed of different radial distances from the circle center. Here 10 lines are shown and in the actual computation we used 100 lines with azimuthal angle distributed evenly from 0 to 2π. The red plus symbol marks the point with the largest B_z in the sunspot. It can be regarded as the center of the sunspot and it is close to the rotation center. **b**, Same as **a** but for the rest of the surface flow, i.e., the curl-free component $\mathbf{v}_2$. **c**, Profile of angular speed at different radial distance from the rotation center. The thin coloured lines denote the values along the corresponding radial lines (by the same colours) as shown in **a**. The thick line (with error bars) denotes the average value (and standard deviation) of angular speed for all the azimuthal angles from 0 to 2π.

as moving magnetic features (Harvey & Harvey 1973), move outward from the sunspots as advected by the moat flow (i.e., the diverging flow existing persistently in the periphery of the sunspot).

Based on the photospheric surface velocity as derived, the rotational speed is estimated in the following way. We first extract the velocity components relevant only to the rotational motion from the surface horizontal velocity $\mathbf{v}$ by decomposing it as

$$\mathbf{v} = \mathbf{v}_1 + \mathbf{v}_2 = \nabla \times \mathbf{p} + \nabla q, \tag{1}$$

where the curl-free part $\mathbf{v}_2 = \nabla q$ is obtained by solving a Poisson equation $\nabla^2 q = \nabla \cdot \mathbf{v}$, and then the divergence-free part is $\mathbf{v}_1 = \nabla \times \mathbf{p} = \mathbf{v} - \mathbf{v}_2$. The rotational flow of the sunspot is contained only in the divergence-free field $\mathbf{v}_1$. Then we estimated the time average of the rotational flow of three days by simply averaging the field $\mathbf{v}_1$ in each pixel using the three-day data of 8–10 September 2014. Figure 4a gives the distribution of the averaged $\mathbf{v}_1$, and Figure 4b shows the averaged $\mathbf{v}_2$. As can be seen, the rotating center is close to the location with the maximum magnetic flux density in the sunspot (also on time average). The curl-free part $\mathbf{v}_2$ shows clearly a diverging flow from approximately the center of the sunspot. With this averaged flow field, we further calculated the rotational rate, i.e., the angular speed of the sunspot with respect to the rotating center. As shown in Figure 4c, we sampled 10 radial lines with different azimuthal angle ϕ (evenly distributed from 0 to 2π) from the center of rotation, and got the rotational velocity $v_\phi(r, \phi)$ on these radial lines. The average angular speed is given by

$$\omega(r) = \frac{1}{2\pi} \int \frac{v_\phi(r, \phi)}{r} d\phi. \tag{2}$$

The angular speed as averaged over three days of 8–10 September 2014 shows that the rotation is the fastest near the center of the sunspot umbra, reaching around $2.5°$ h^{-1}, and it decreases gradually to zero outside of the penumbra at a radial distance of 25 Mm (Figure 4c). When averaged for the whole sunspot, the rotation speed is about $1.75°$ h^{-1} (see Figure 1e), and thus in the three days the sunspot has rotated with a total degree of $\sim 130°$. Our result of the total rotation degree for the three days from 8–10 September 2014 agrees well with the value obtained from other independent methods for the same sunspot (Brown & Walker 2021; Vemareddy et al. 2016).

3. NUMERICAL MODEL

To simulate the quasi-static slow evolution of the AR until its fast eruption, we selected 00:00 UT on 8 September 2014, a time over 65 hours before onset of the X1.6 flare, as a starting point. We first constructed an MHD equilibrium based on a single vector magnetogram taken by the SDO/HMI for the starting time, using an MHD-relaxation technique (Jiang et al. 2021a). The MHD equilibrium represents a snapshot of coronal evolution at that time. Then, with this well-established equilibrium as the initial condition, we carried out MHD simulation as driven by surface motions specified at the bottom boundary by assuming that the major

sunspot rotates like a rigid body (namely with a constant angular speed within the sunspot, which is the simplest case) while all other regions are fixed, therefore emphasizing the effect of sunspot rotation in leading to the eruption.

3.1. *Model equations*

The simulation is carried out by solving numerically the MHD equations as follows, using an advanced conservation element and solution element (CESE) method (Feng et al. 2007; Jiang et al. 2010),

$$\begin{aligned}\frac{\partial \rho}{\partial t}+\nabla\cdot(\rho\mathbf{v})&=-\nu_\rho(\rho-\rho_0),\\ \rho\frac{d\mathbf{v}}{dt}&=-\nabla p+\mathbf{J}\times\mathbf{B}+\rho\mathbf{g}+\nabla\cdot(\nu\rho\nabla\mathbf{v}),\\ \frac{\partial \mathbf{B}}{\partial t}&=\nabla\times(\mathbf{v}\times\mathbf{B}),\\ \frac{\partial T}{\partial t}+\nabla\cdot(T\mathbf{v})&=(2-\gamma)T\nabla\cdot\mathbf{v}. \end{aligned}\tag{3}$$

where the electric current density $\mathbf{J}=\nabla\times\mathbf{B}$, ν is the kinetic viscosity, and γ is the adiabatic index. Note that the equations are written in non-dimensional form with all variables normalized by their typical values at the base of the corona, which are, respectively, density $\rho_s = 2.29\times10^{-15}$ g cm^{-3}, temperature $T_s = 10^6$ K, velocity $v_s = 110$ km s^{-1}, magnetic field $B_s = 1.86$ G, length $L_s = 11.52$ Mm, and time $t_s = 105$ s.

In this simulation, an artificial source term $-\nu_\rho(\rho-\rho_0)$ has been added to the continuity equation (i.e., the first equation in Equations (3)), where ρ_0 is the density at the initial time $t = 0$, and ν_ρ is a prescribed coefficient given as $\nu_\rho = 0.05v_{\rm A}$ ($v_{\rm A} = B/\sqrt{\rho}$ is the Alfvén speed). This term is used to avoid ever decreasing of the density in the strong magnetic field region, an issue often encountered in simulations handling very large magnetic field gradients and at the same time with very low plasma β (Jiang et al. 2021a). It can maintain the maximum Alfvén speed in a reasonable level, which may otherwise increase and make the iteration time step smaller and smaller and the long-term simulation unmanageable. This source term is actually a Newton relaxation of the density to its initial value by a time scale of

$$\tau_\rho=\frac{1}{\nu_\rho}=20\tau_{\rm A},\tag{4}$$

where $\tau_{\rm A} = 1/v_{\rm A}$ is the Alfvén time with length of 1 (the length unit L_s). Thus it is sufficiently large to avoid influence on the fast dynamics of Alfvénic time scales. We have run test simulations with much larger values of τ_ρ, which give almost the same evolution in both kinetic and magnetic energies, but the time step decreases substantially and therefore the whole simulation will demand a much longer computational time. Using a diffusion term of the density to smooth its profile has also been considered in other simulations for the same purpose (Aulanier et al. 2010, 2005).

Similar to our previous works (Jiang et al. 2021c,a), we chose to not use explicit resistivity in the magnetic induction equation, but magnetic reconnection can still be triggered through numerical diffusion when a current layer is sufficiently narrow (and thus the current density will be sufficiently large) with thickness close to the grid resolution. By this, we achieved an effective resistivity as small as we can with a given grid resolution, and also mimicked the current-density-dependent resistivity as required for fast Petscheck-type reconnection, because the resistivity is not uniform in the whole computational volume, and only when the current density is sufficient large the resistivity will be effective, while otherwise it is almost negligible. For simplicity, the adiabatic index is set as $\gamma = 1$ in the energy (or temperature) equation, which thus reduces to an isothermal process. Although in this case we can simply discard the energy equation by setting the temperature as a constant, we still keep the full set of equations in our code and can thus describe either the isothermal or adiabatic process by choosing particular values of γ. The kinetic viscosity ν is given with different values when needed, which is described in the following sections.

3.2. *Construction of an initial MHD equilibrium*

To initialize the surface flow-driven simulations, an MHD equilibrium is constructed based on the SDO/HMI vector magnetogram taken for time of 00:00 UT on 8 September 2014. Such an equilibrium is assumed to exist when the corona is not in the eruptive stage, and is crucial for starting our subsequent surface flow-driven evolution. Beforehand we preprocessed the vector magnetogram use a method developed by Jiang & Feng (2014) and further smoothed all the three components of the magnetic field using Gaussian smoothing with FWHM of 6 arcsec. This is done for two reasons: on the one hand, the preprocessing minimizes the photospheric Lorentz force contained in the vector magnetogram, which is helpful for reaching a more force-free equilibrium state (Wiegelmann et al. 2006); on the other hand, the smoothing effectively filters out the small-scale magnetic structures that cannot be sufficiently resolved in our simulation, and it also mimics the effect of magnetic field expansion from the photosphere to the base of the corona (Yamamoto & Kusano 2012), since the lower boundary of our simulation is assumed to be the coronal base rather than directly the photosphere (Jiang & Toriumi 2020; Jiang et al. 2016).

We constructed the MHD equilibrium based on an MHD-relaxation approach consisting of two steps (Jiang et al. 2021a). In the first step, a potential magnetic field $\mathbf{B}_{\rm pot}$ extrapolated from the vertical component (i.e., $\mathcal{B}_z$) of the preprocessed and smoothed vector magnetogram ($\mathcal{B}_x, \mathcal{B}_y, \mathcal{B}_z$), along with an initial plasma as the background atmosphere

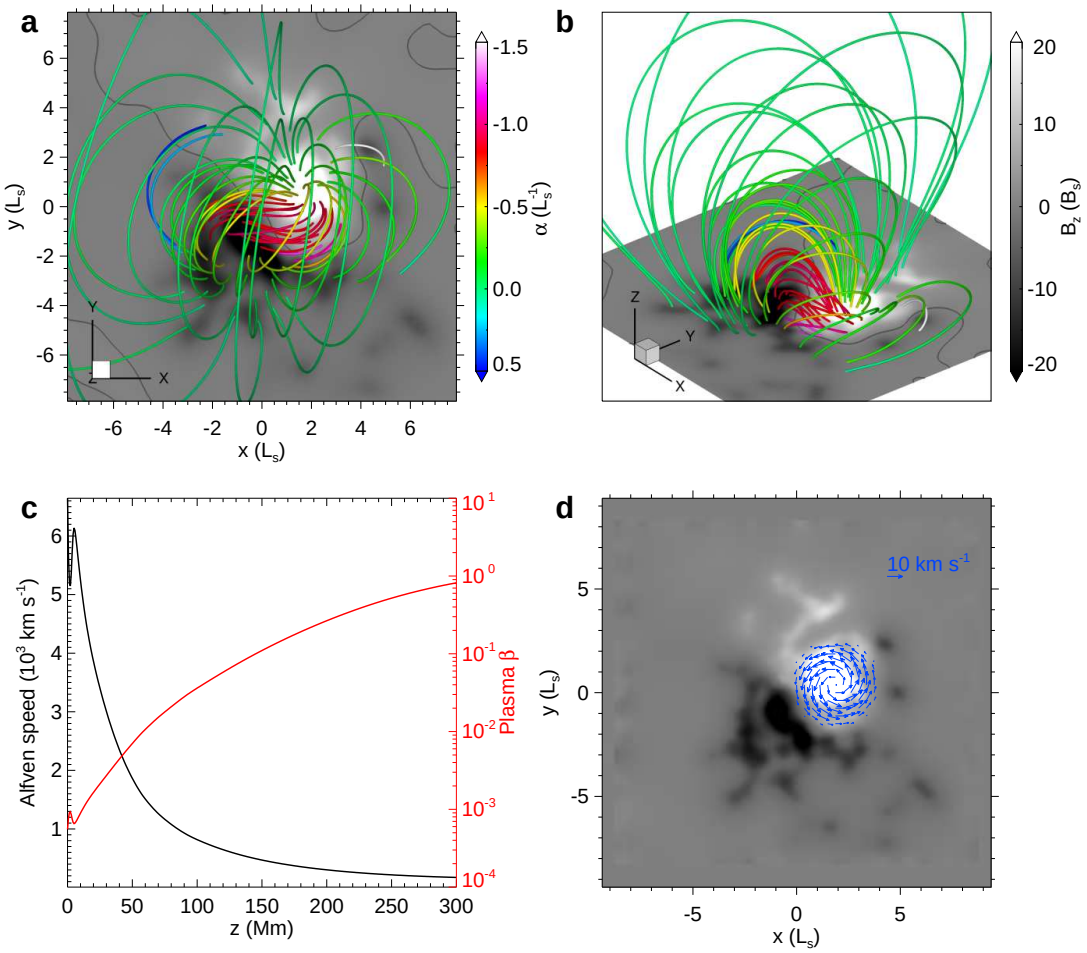

Figure 5. The initial state of the simulation. a, Magnetic field lines as seen from above. The field lines are false-colored by the values of the force-free factor $\alpha = \mathbf{J} \cdot \mathbf{B}/B^2$. The background is shown by the magnetic flux distribution on the bottom surface, and the thick gray curves are shown for the PIL, i.e., where $B_z = 0$. **b**, Same as **a** but seen in a 3D perspective view. **c**, Profiles of Alfvén speed and plasma β with height along a vertical line with footpoint at the center of the main sunspot. **d**, The rotational flow at the bottom surface as used in the simulation with rigid rotation of the sunspot. The background is shown by the magnetic flux distribution.

were input into the MHD model. For the initial plasma, we used an isothermal gas in hydrostatic equilibrium. It is stratified by solar gravity with a density $\rho = 1\rho_s$ at the bottom and a uniform temperature of $T = 1T_s$. With the plasma configured by typical coronal density and temperature, we chose to reduce the original magnetic field strength by a factor of 20, such that the maximum of magnetic field strength in normalized value is approximately $50 \sim 100$ in the model. If using the original values of magnetic field, its strength (and the characteristic Alfvén speed) near the lower surface is too large, and will put a too heavy burden on computation since the time step of our simulation is limited by the Courant-Friedrichs-Lewy (CFL) condition.

With these initial conditions, we modified the transverse magnetic fields on the bottom boundary incrementally in time (using linear extrapolation with a duration of $t = 1t_s$) from that of the potential field $\mathbf{B}_{\rm pot}$ to that of the vector magetogram $(\mathcal{B}_x, \mathcal{B}_y, \mathcal{B}_z)$. The process drives the coronal magnetic field to evolve away from the initial potential state, since the change of the transverse field injects electric currents and thus Lorentz forces, which induce motions in the computational volume. In this phase all other variables on the bottom boundary are simply fixed, thus the plasma remains to be motionless there. Although this procedure is somewhat un-physical since the Lorentz force will also introduce nonzero flows on the bottom boundary, it provides a simple and 'safe' way (avoiding numerical instability) to bring the transverse magnetic field into the MHD model. Once the magnetic field on the bottom surface is identical to that of $(\mathcal{B}_x, \mathcal{B}_y, \mathcal{B}_z)$, the MHD system is then allowed to relax to an equilibrium with all the variables (including the magnetic field) on the bottom boundary fixed. To avoid a too large velocity in this phase such that the system can relax fast, we set a relatively large kinetic viscosity coefficient,

which is given by $\nu = 0.5\Delta x^2/\Delta t$ (where Δx is the local grid spacing and Δt the local time step as determined by the CFL condition with the fastest magnetosonic speed). Actually this is the largest viscosity one can use with a given grid size Δx and time step Δt, because the CFL condition for a purely diffusive equation with diffusion coefficient ν requires $\Delta t \leq 0.5\Delta x^2/\nu$. The relaxation phase takes a time of $t = 20t_s$ with the average relative residual of magnetic field in the whole volume between two consecutive time steps reduced to a sufficiently small level of below 10^{-5}.

In the second step, we carried out a 'deeper' relaxation by running the model again but started with the relaxed magnetic field obtained in the first step and the initially hydrostatic plasma. We reduced the kinetic viscosity to $\nu = 0.05\Delta x^2/\Delta t$, i.e., an order of magnitude smaller than that used in the first step, which corresponds to a Reynolds number of 10 for the length of a grid cell Δx. Furthermore, the magnetic field at the bottom boundary is allowed to evolve in a self-consistent way with assumptions that the bottom boundary is a perfectly line-tying and fixed (i.e., $\mathbf{v} = 0$) surface of magnetic field lines. Note that such a line-tying condition does not indicate that all magnetic field components on the boundary are fixed, because even though the velocity $\mathbf{v}$ is given as zero on the bottom boundary, it is not necessarily zero in the neighboring inner points. To self-consistently update the magnetic field, we solve the magnetic induction equation on the bottom boundary. Slightly different from the one in the main equations (3), the induction equation at the bottom surface is given by

$$\frac{\partial \mathbf{B}}{\partial t} = \nabla \times (\mathbf{v} \times \mathbf{B}) + \eta_{\rm p} \nabla_\perp^2 \mathbf{B}, \tag{5}$$

where we added a surface diffusion term defined by a surface Laplace operator as $\nabla_\perp^2 = \frac{\partial^2}{\partial x^2} + \frac{\partial^2}{\partial y^2}$ with a small resistivity for numerical stability near the polarity inversion line (PIL) $\eta_{\rm p} = 1 \times 10^{-3} e^{-B_z^2}$, since the photospheric magnetic fields often have the strongest gradient across the main PIL. The surface induction Equation (5) in the code is realized by second-order difference in space and first-order forward difference in time. Specifically, on the bottom boundary (we do not use ghost cell), we first compute $\mathbf{v} \times \mathbf{B}$, and then use central difference in horizontal direction and one-sided difference (also 2nd order) in the vertical direction to compute the convection term $\nabla \times (\mathbf{v} \times \mathbf{B})$. The surface Laplace operator is also realized by central difference.

Figure 5a and b shows the 3D magnetic field lines of the final relaxed MHD equilibrium, which has a small ratio of kinetic energy to magnetic energy of below 10^{-3}. Note that the field lines are pseudo-colored by the values of the force-free factor defined as $\alpha = \mathbf{J} \cdot \mathbf{B}/B^2$, which indicates how much the field lines are non-potential. For a force-free field, this parameter is constant along any given field line. As can be seen, the magnetic field is close to a force-free one since the color is nearly the same along any single field line. In the core of the configuration, the field lines are sheared significantly along the PIL, thus having large values of α and current density. On the other hand, the overlying field is almost current-free or quasi-potential field with $\alpha \sim 0$, and it plays the role of strapping field that confines the inner sheared core. Figure 5c shows the profile of plasma β and Alfvén speed with height, as an example, along a vertical line with footpoint at the center of the main sunspot. The largest Alfvén speed is more than 6×10^3 km s^{-1}, and the plasma β is mostly smaller than unity below 300 Mm with the smallest value of 5×10^{-4}, therefore characterizing well the essential conditions of dynamics in the corona, i.e., very large Alfvén speed and low plasma β.

3.3. *Rigid rotation of the sunspot*

To mimic the observed rotational profile of the sunspot in a simple way, the sunspot is rotated rigidly with respect to its surrounding field by applying a velocity profile at the bottom boundary defined as

$$v_x = -\omega(y - y_c), \;\; v_y = \omega(x - x_c) \tag{6}$$

where the rotating center (x_c, y_c) is defined to be the point in the sunspot with the largest B_z, and the angular speed ω is a constant (positive, thus rotating counter-clockwise) within a radius of 10 arcsec from the rotating center, and then decreases linearly to zero at a radius of 35 arcsec. The value of ω is scaled such that the maximum value of the surface speed is 10 km s^{-1}. Figure 5d shows the distribution of the surface flow. The implementation of the bottom boundary conditions is the same as that for the second step (the deeper relaxation phase) described in Section 3.2. That is, on the bottom surface, we solved the Equation (5) to update all the three components of magnetic field with the flow field prescribed by those defined in Equation (6), while the plasma density and temperature are simply fixed.

3.4. *Grid setting and numerical boundary conditions*

For the purpose of minimizing the influences introduced by the side and top numerical boundaries of the computational volume, we used a sufficiently large box of $(-32, -32, 0)L_s < (x, y, z) < (32, 32, 64)L_s$ embedding the field of view of the magnetogram of $(-8.75, -8.25)L_s < (x, y) < (8.75, 8.25)L_s$, and the simulation runs are stopped before the disturbance by the eruption reaches any of the side and top boundaries. The full computational volume is resolve by a non-uniform block-structured grid with adaptive mesh refinement (AMR), in which the highest and lowest resolution are $\Delta x = \Delta y = \Delta z = 1/16L_s$ (corresponding to 1 arcsec or 720 km, matching the resolution of the vector magnetogram) and $1/2L_s$, respectively. The AMR is controlled to resolve with the smallest grids the regions of strong

magnetic gradients and current density, particularly near the current sheet. The magnetic field outside of the area of the magnetograms on the lower boundary is given as zero for the vertical component and simply fixed as the potential field for the transverse components. On the side and top boundaries, since the simulation runs are stopped before the disturbance by the eruption reaches any of these boundaries on which all the variables do not evolve, we thus fixed the plasma density, temperature, and velocity as being their initial values. But to avoid numerical errors of magnetic divergence accumulated on these boundaries, the tangential components of magnetic field are linearly extrapolated from the inner points, while the normal component is modified according to the divergence-free condition.

4. SIMULATION RESULTS

The simulation demonstrates an evolution from an initially quasi-static stage to finally a fast eruption. The evolutions of 3D structure of magnetic field and electric current before the eruption are shown in Figures 6 and 7, while their evolutions during eruption are given in Figure 8, and the time profiles of the magnetic and kinetic energies in the whole process, along with the kinematic behaviour of the erupting features, are plotted in Figure 9. Below we describe the different stages and the key processes in the simulated MHD evolution.

4.1. *The pre-eruption stage*

The magnetic configuration at the initial time is a sheared arcade core enveloped by an overlying, nearly current-free field. As the main sunspot rotates counterclockwise, the coronal magnetic configuration expands slowly and the degree of magnetic shear increases, i.e., with the field lines in the core part becoming more and more aligned with the bottom PIL as viewed from above (Figure 6a and its animation). Progressively, these field lines, as a whole, form a prominent reverse S shape. To mimic the emission of the structure, we generated synthetic images of coronal emission from current density using a method similar to that proposed in ref Cheung & DeRosa (2012). Since it is commonly believed that the coronal loops generally reflect the structure of the magnetic field lines rooted in the photosphere, we first traced a sufficiently large number ($\sim 10^6$) of field lines with their footpoints uniformly distributed at the bottom surface. All the field lines are traced with fixed step of 720 km. Then on each field line, all the line segments are assigned with a proxy value of emission intensity represented by the averaged square of current density along this field line, by simply assuming that the Ohmic dissipation of the currents heats the corona. Finally, the total emission along the line of sight (here simply along the z axis) is obtained by integrating all the emission intensity along the z axis, which forms the final synthetic image. As shown in Figure 6c, a sigmoid structure is also seen in the synthetic images of coronal emission from current density. It resembles the observed coronal sigmoid structure, for example, comparing the last image of Figure 6c with the EUV sigmoid as shown in Figure 1b. In the pre-flare phase from $t = 0\ t_s$ to $t = 20\ t_s$ (where $t_s = 105$ s is the time unit used in the numerical model), the magnetic energy increases monotonically with a nearly constant rate (Figure 9a), because the sunspot rotates with a constant speed. While the magnetic energy rises significantly, the kinetic energy keeps a small value of around $1 \times 10^{-3} E_0$ (where E_0 is the potential field energy at the initial time), and thus most of the injected energy from the bottom boundary through the surface driving motion (which is indicated by the red dashed line in Figure 9a) is stored as coronal magnetic energy. Moreover, since the rotation motion introduces very limited variation to the magnetic flux distribution at the bottom surface and thus the corresponding potential-field energy changes only slightly during the whole evolution process (the black dashed line in Figure 9a), most of the injected energy is stored as free magnetic energy in the corona. A total amount of free energy of $\sim 0.5\ E_0$ has been stored until the eruption onset at $t = 28\ t_s$, and thus the non-potentiality, as measured by the ratio of the total magnetic energy to the potential field energy, reaches 1.9. Meanwhile, the sunspot has rotated by about $115°$, which is almost identical to that derived from observations ($\sim 114°$), i.e., an average rotational rate of $1.75°$ h^{-1} (as shown in Figure 1) multiplied by a time of 65 h before the X1.6 flare. If not interrupted by the eruption, it seems that with another $100°$ of rotation the non-potentiality can approach an upper limit of approximately $2.45\ E_0$ as determined by the fully open field (Aly 1991; Sturrock 1991). But such ideal evolution is not possible because a central current sheet unavoidably forms and triggers reconnection, which results in the eruption.

4.2. *Formation of a current sheet*

A clear signature of current sheet formation can be seen in the evolution of current density in cross sections of the volume (Figure 7 and the animation of Figure 6). Note that the current density is normalized by the magnetic field strength (i.e., J/B) to emphasize thin layers with strong current. Initially the current density is volumetric, and gradually a narrow layer with enhanced density emerges, becomes progressively thinner. To characterize this evolution of the current layer, we have measured its thickness, which is defined at the location where it is thinnest. As can be seen in the variation of the current layer thickness with time in Figure 9b, the thickness of the current layer decreases all the way until the onset of the eruption. At the time of $t = 28\ t_s$, the thin current layer extends from the bottom to a height of 50 Mm with a thickness of around 3Δ (here $\Delta = 0.72$ Mm is the finest

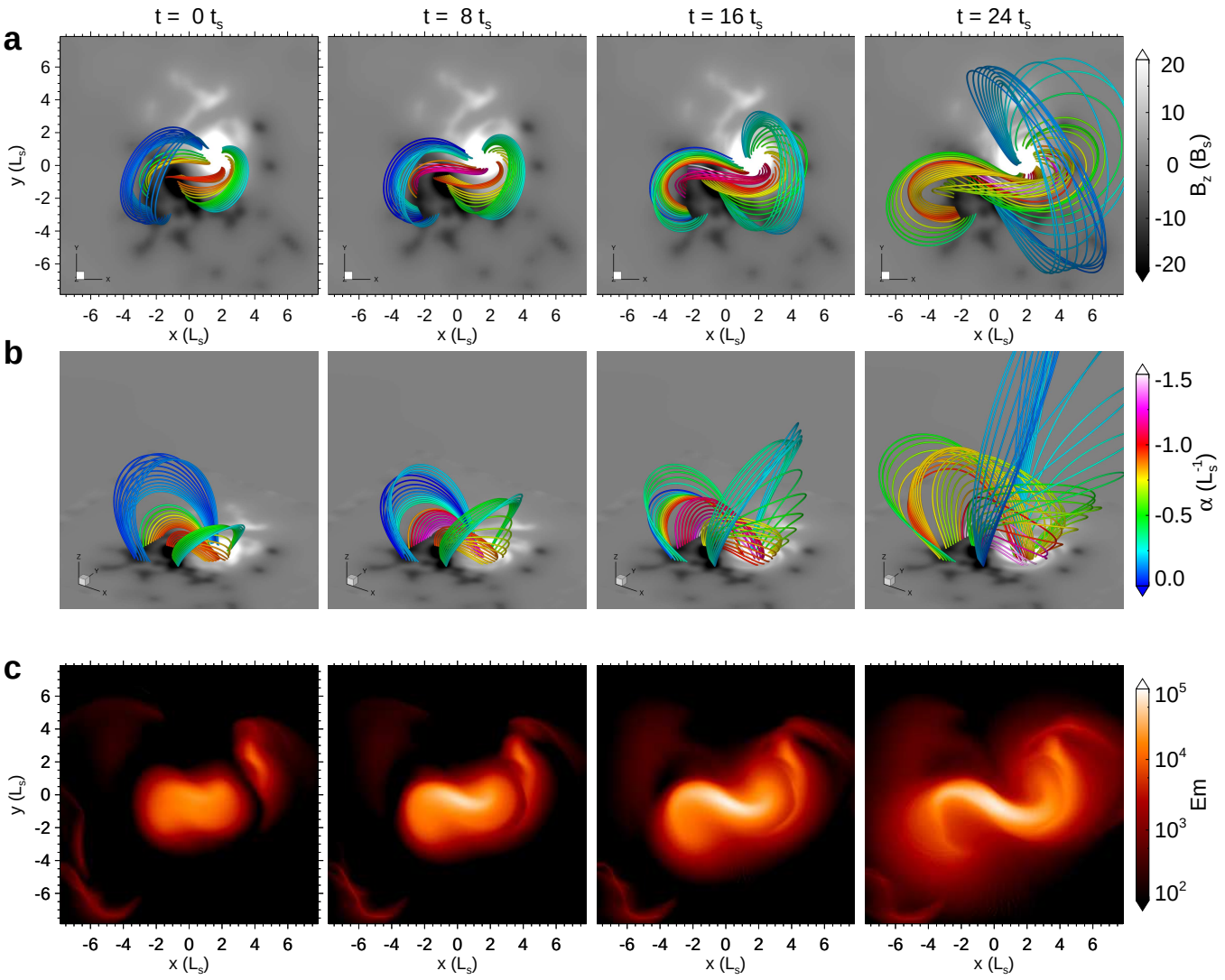

Figure 6. Pre-eruption evolution of magnetic field and current density in the simulation. a, Top view of sampled magnetic field lines. The coloured thick curves represent magnetic field lines, and the colours denote the value of the nonlinear force-free factor defined as $\alpha = \mathbf{J}\cdot\mathbf{B}/B^2$ where $\mathbf{J}$ is the current density and $\mathbf{B}$ is the magnetic field. The background shows the magnetic flux distribution on the bottom surface. Note that at different times, the field lines are traced from the same set of footpoints from the negative polarities, since they are fixed without surface motion during the simulation with the rigid rotation. $L_s = 11.52$ Mm is the length unit, $t_s = 105$ s the time unit, and $B_s = 1.86$ G the magnetic field strength unit. **b**, 3D prospective view of the same field lines shown in **a**. **c**, Synthetic images of coronal emission from current density. The attached animation shows evolution of magnetic field lines (left), current density (middle), and magnetic squashing factor (right) in the simulation (for the core region). The left two panels and correspond to the animation versions of Figure 6**a** and **b**, respectively, and the middle top panel corresponds to Figure 6**c**. The bottom middle and right panels correspond to Figure 7**a** and **b**, respectively. The top right panel corresponds to Figure 8**c**.

grid resolution). This is the critical time point when the current sheet reaches beyond the grid resolution and the numerical resistivity arises to trigger fast reconnection in the current sheet, which initiates the eruption. The current sheet formation is accompanied with the formation of a quasi-separatrix layer (QSL (Démoulin et al. 1996)) as seen in the distribution of the magnetic squashing degree (i.e., Q factor, see Figure 7b and d). The Q factor quantifies the gradient of magnetic field-line mapping with respect to their footpoints, and it is helpful for searching topological interface or QSLs of magnetic flux connections using extremely large values of Q factor ($\sim 10^5$) (Titov et al. 2002; Liu et al. 2016). Initially the Q factor distributes smoothly with mostly small values. Along with narrowing of the central current layer, there is an evident increase of Q in the central thin layer. Immediately prior to the eruption, it has Q reaching $\sim 10^5$ and an extremely small thickness, thus being identified as QSL, at the same location with the enhanced values of J/B.

4.3. *The eruption and reconnection*

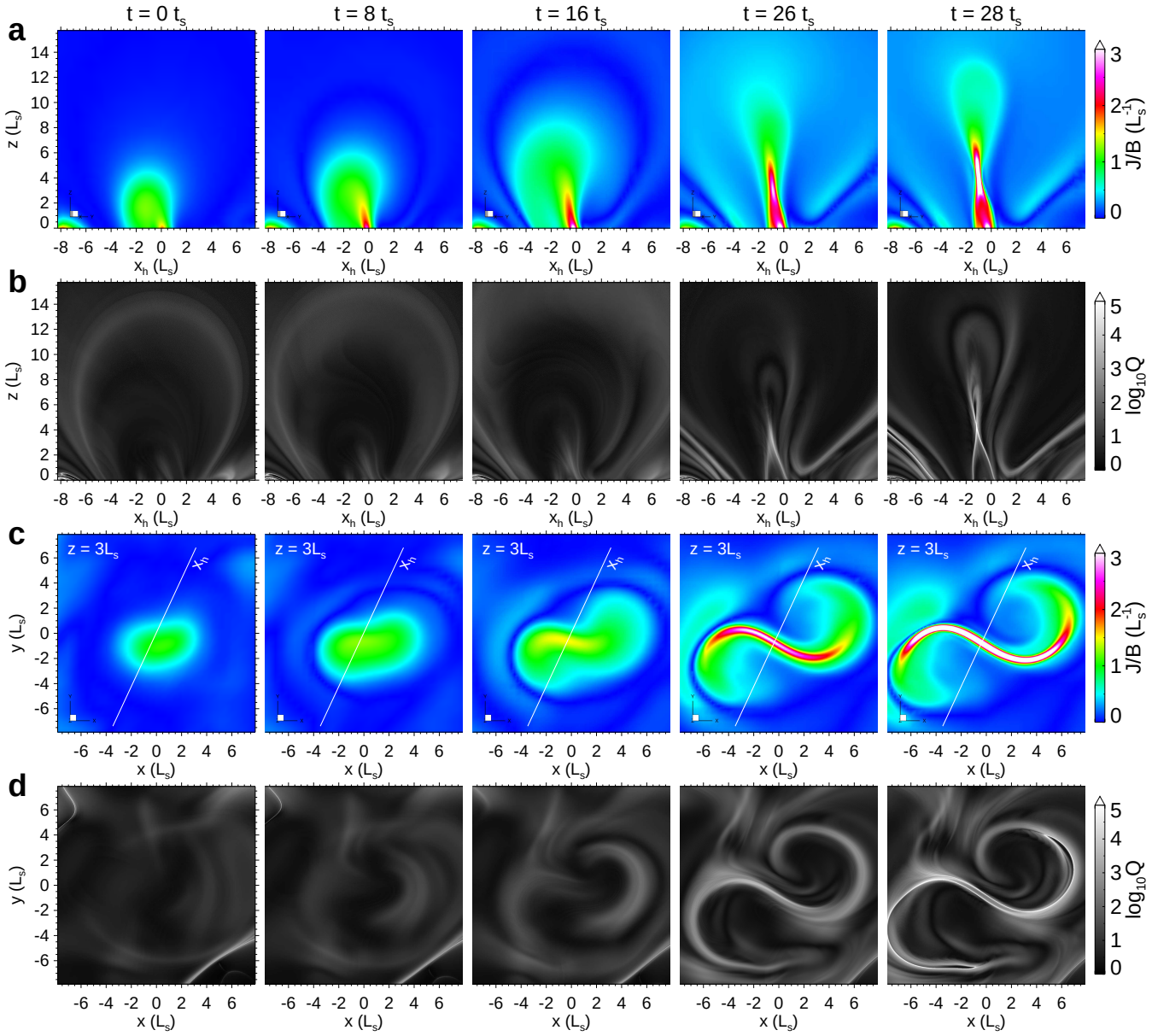

Figure 7. Formation of the current sheet in the pre-eruption evolution phase of sunspot rigid-rotation simulation. **a**, Vertical cross-section of the normalized current density, namely, J/B. **b**, Distribution of magnetic squashing degree (i.e., Q factor) on the same slice of **a**. **c**, Horizontal cross-section of the normalized current density at a fixed height of $z = 3L_s$. The projected location of the vertical cross-section in **a** and **b** is denoted by the black line in **c**, which crosses through the current sheet perpendicularly at the point with the highest current density. **d**, Distribution of Q factor on the same slice of **d**.

With onset of the eruption, the kinetic energy increases impulsively and reaches finally about $0.07\ E_0$, while the total magnetic energy experiences a fast decrease, even though the boundary driving still injects magnetic energy into the volume. The total released magnetic energy amounts to $0.3\ E_0$ or 4×10^{32} erg if scaled to the realistic value of the magnetic field, which is sufficient to power a typical X-class flare (Emslie et al. 2012). The eruption of the magnetic field creates a large-scale MFR through the continuous magnetic reconnection in the current sheet (Figure 8 and its animation). The existence of such an MFR in this event has been confirmed by in-situ observation in the interplanetary space of the CME from this AR (Kilpua et al. 2021). Ahead of the MFR, the eruption drives a fast magnetosonic shock, which is shown by the thin arc of the current density on the top of the MFR. During the eruption, the reconnecting current sheet extends in both transverse size and height, but is kept in the same thickness that is allowed by the given grid resolution (Figure 8b and Figure 9b). When using an sufficiently high resolution such that the Lundquist number of the cur-

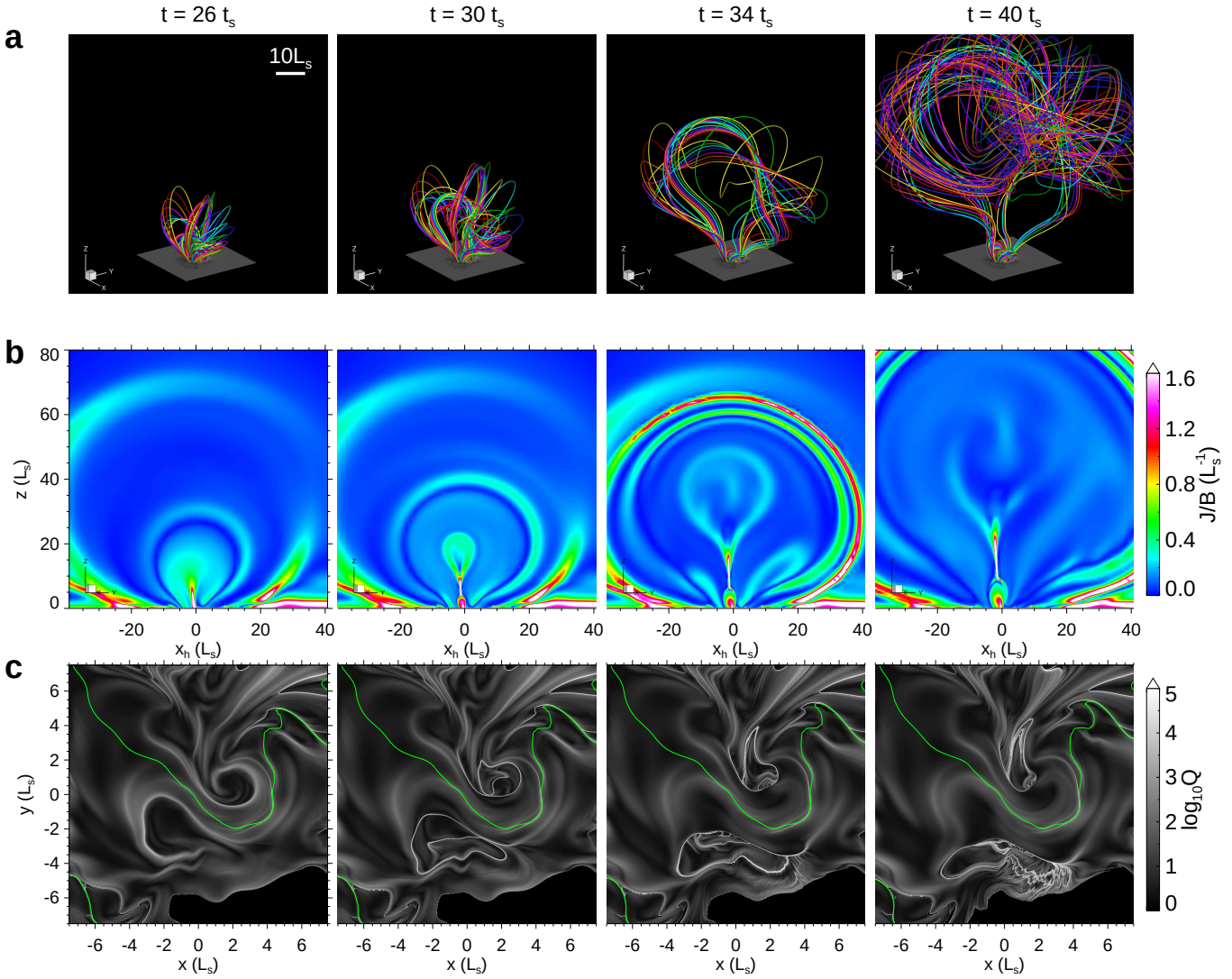

Figure 8. Evolution of the erupting field in the sunspot rigid-rotation simulation. **a**, Magnetic field lines are shown by the thick coloured lines, and the colours are used for a better visualization of the different lines. The bottom surface is shown with the distribution of magnetic flux. The field lines at different times are traced from the same set of footpoints from the negative polarities, since they are fixed without surface motion during the simulation with rigid rotation. **b**, Vertical central cross-section of the normalized current density. Location of the cross section is the same one as shown in Figure 7a. Note that there are two thin current layers on top of the erupting MFR (seen at $t = 34\ t_s$), and the shock refers to the outermost one. This layer is not related to the topology interface or QSL of the field lines. The current layers immediately below the shock is a QSL and it is formed well before the shock forms. **c**, Magnetic squashing factor at the bottom surface. The green curves represent the magnetic polarity inversion line. An animation is attached for **a** and **b** of this figure.

rent sheet can reach the order of $10^4 \sim 10^5$, the reconnecting current sheet would run into plasmoid instability and could then trigger turbulence, which help to achieve a fast reconnection rate (Bhattacharjee et al. 2009; Daughton et al. 2011; Jiang et al. 2021c). For the current simulation, we have also carried out an experiment with much higher resolution of $\Delta = 90$ km, and indeed the plasmoid instability is triggered as shown in Figure 10. Since the high-resolution run requires an extremely long computational time, it is performed for only a short period during the eruption from $t = 30.5\ t_s$ to $33.5\ t_s$.

Connecting to the bottom of the current sheet is a cusp structure, below which is the post-flare arcade, i.e., the short field lines formed after the reconnection. The post-flare arcade and the MFR are separated, initially partially but later fully, by the QSL that originates from the current sheet and forms the topological surface of the MFR (Jiang et al. 2021b). The QSL exhibits two J-shaped footprints at the bottom surface (Figure 8c), and these footprints consists of the limits of the MFR (i.e., the hook parts of the QSL footprints) and the footpoints of the field lines that are undergoing reconnection in the current sheet (mainly the leg parts), and the latter are believed to correspond to the location of flare ribbons.

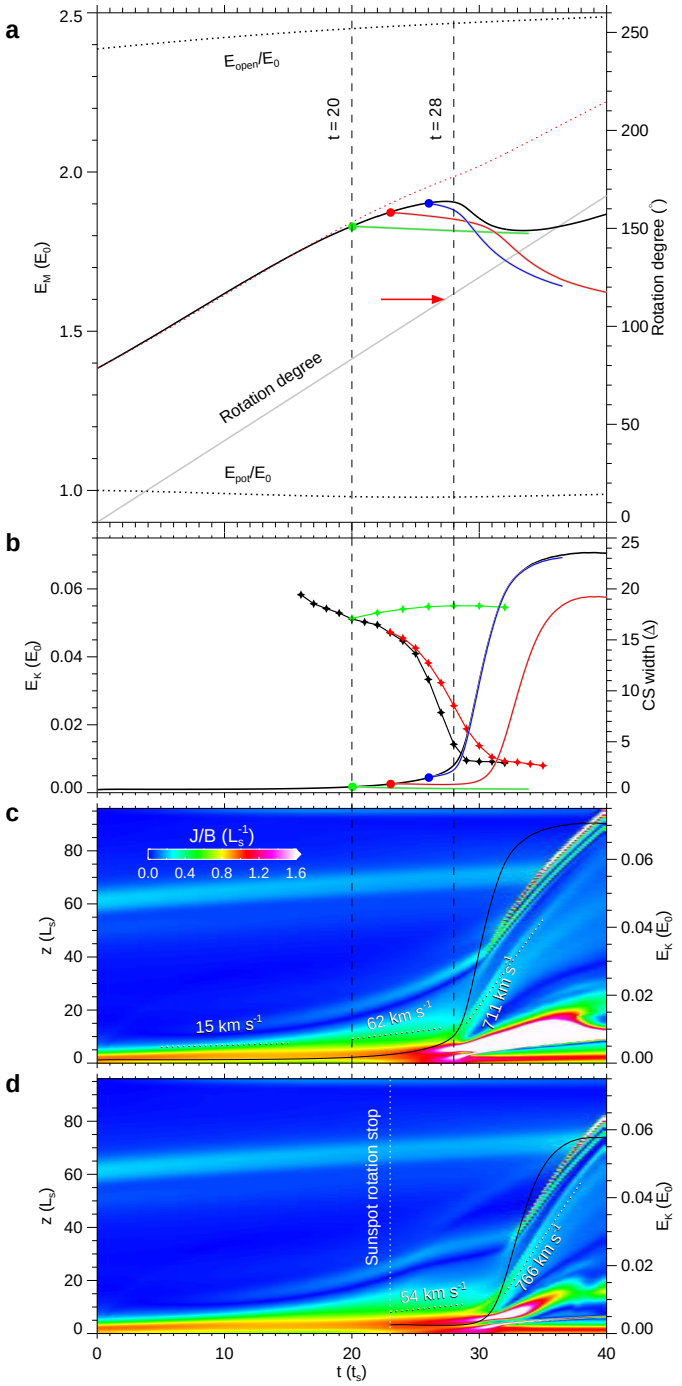

Figure 9. Temporal evolution of different parameters in the simulation with rigid rotation of sunspot. **a**, Magnetic energies are shown with the left y-axis. The black line shows result with continuous rotation. The red dashed line shows the energy injected into the volume from the bottom boundary through the surface rotational flow, that is, a time integration of total Poynting flux at the bottom surface. The green, red, and blue lines show results of runs with the rotation switched off at $t = 20\ t_s$, $23\ t_s$, and $26\ t_s$, respectively. All the energies are normalized by the initial potential field energy E_0, which is 3.04×10^{30} erg in the simulation, and is 1.22×10^{33} erg if scaled to the realistic value. The two black dashed lines show evolution of the energies of the open field (the upper one) and the potential field (the lower one). The gray line shows the rotational degree with the right y-axis. The red arrow denotes the total rotation degree from the initial time to flare onset as derived from observation. **b**, Kinetic energies (solid lines) with the left y-axis, and thickness of the current layer (solid lines with stars) with the right y-axis. Same as in **a**, the line colored in black, green, red, and blue show results of the continuous rotation run, and runs with the sunspot rotation stopped at $t = 20\ t_s$, $23\ t_s$, and $26\ t_s$, respectively. **c**, A time stack map of the J/B distribution around $x, y = 0$ for the continuous rotation run, which is used to show the evolution speed of the erupting structure. **d**, The same time stack map of J/B distribution as **c** but for the simulation run with sunspot rotation stopped at $t = 23\ t_s$. The typical speed of the structures are denoted by the dashed lines. The animation attached for this figure has the same format as the animation of Figure 8, but for the simulation with the sunspot rotation stopped at $t = 23\ t_s$.

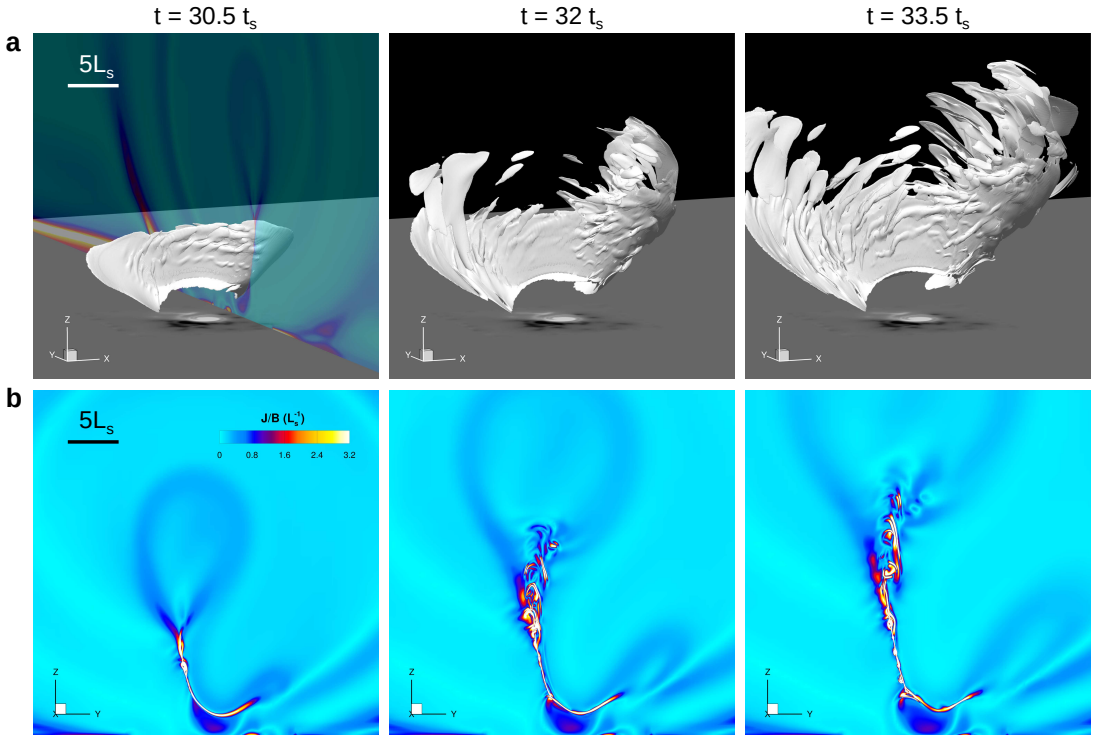

Figure 10. A high-resolution simulation of the eruption process with the plasmoid instability triggered in the flare current sheet. The grid resolution of the current sheet reaches 90 km, eight times higher than the main run. **a**, The 3D structure of the flare current sheet as shown by the iso-surface of $J/B = 3.2L_s^{-1}$. The bottom surface is shown with the distribution of magnetic flux. **b**, A vertical slice of current sheet, for which the location is denoted in the first panel of **a**.

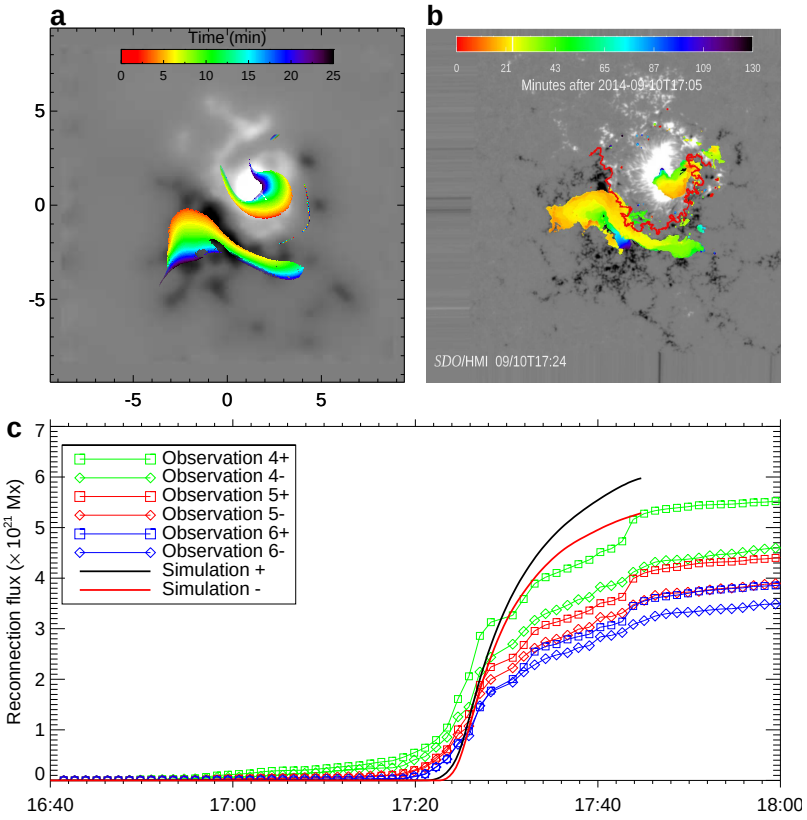

Figure 11. Comparison of reconnection fluxes derived from simulation and observation. a, Temporal and spatial distribution of simulated "flare ribbons", which are the footpoint locations of the newly reconnected field lines that forms the closed short arcades corresponding to the post-flare loops. The color denotes the time of minutes after the simulation eruption onset time. The background gray image shows the magnetic flux distribution at the bottom surface. **b**, Format same as **a** but for the observed flare ribbons as imaged in SDO/AIA 1600 Å wavelength. **c**, Evolution of reconnection flux, which is the sum of the magnetic flux in the area swept by the flare ribbons. For the simulation, the fluxes are counted for the positive (the thick black line) and the negative (the thick red line) polarities separately. For the observed data, three sets of results are obtained by different background removal criteria for selection of the flare ribbons, which are pixels with the intensity larger than 4 (green line), 5 (red line), and 6 (blue line) times of the background average brightness. The line with boxes (diamonds) represent values counted for the positive (negative) polarity.

Indeed, the shape and evolution of the QSL footprints are in reasonable consistence with that of the observed flare ribbons in SDO/AIA 1600 Å, by taking into consideration of the systematic difference of the photospheric magnetic field between the simulation and observation. By tracing the movement of the QSL footprints, one can compute the evolution of the reconnection flux, which is the magnetic flux as swept by the moving QSL footprints. Figure 11 shows that the results, in both the reconnection flux and the reconnection rate, are comparable to those derived from evolution of the observed flare ribbons (He et al. 2022). Note that there are also reconnection within the MFR (Jiang et al. 2021b), and this reconnection creates field lines with higher twist number than that created by the initial tether-cutting reconnection. As a result, these field lines are separated with others by the newly-formed embedded QSLs in each hook, which are similar to the ones described in an analytic study (Démoulin et al. 1996).

4.4. *The pre-eruption slow rise phase*

Although Figure 9 shows a typical slow storage of magnetic free energy to its fast release in eruption, the evolution can actually be divided into three different stages, that is, a quasi-static phase, an impulsive rise phase, and a slow rise phase in between, which is likely to correspond to the observed short period of coronal loop slow expansion immediately before the eruption. The first phase from the beginning to around $t = 20\ t_s$ is truly quasi-static because, on the one hand, the core field expands with a speed close to that of the bottom driving speed (Figure 9c), and on the other hand, at any instant in this phase, if we stop the bottom driving (i.e., by turning off the rotation of the sunspot), the system can relax smoothly to an equilibrium with gradual decline of the kinetic energy. For instance, the kinetic energy keeps decreasing once the rotation is switched off at $t = 20\ t_s$. In the quasi-static phase, almost all the magnetic energy injected

from the bottom boundary is stored in the coronal volume, as shown by the close match of the energy injection line (the gray curve in Figure 9a) and the evolution profile of the total magnetic energy. Clearly, the time scale of the quasi-static evolution depends on that of the bottom driving. Since we used a surface speed (of about 10 km s^{-1}) larger than the actual photospheric motion speed, the quasi-static phase in our simulation (with a duration of 20 $t_s \approx 0.6$ hours) is much shorter than the realistic one (nearly 60 hours). It can be scaled approximately to the realistic one if we use the realistic speed (for example, on the order of 0.1 km s^{-1}) of the photospheric motion, but that demands too much computing time.

The second phase from around $t = 20\ t_s$ to the onset time of eruption (i.e., 28 t_s) is a slow rise phase, in which the kinetic energy slowly rises and the magnetic energy evolution begins to deviate evidently from the magnetic energy injection curve. This phase is also featured by a relatively large speed of $50 \sim 60$ km s^{-1} as shown in the expansion rate of the core field. A more important reason why this phase is different from the first phase in nature is that, if the bottom driving is turned off at any moment in this phase, the system will not relax to a static equilibrium (for example, see the evolution of the kinetic energy when the surface driving is turned off at $t = 23\ t_s$ in Figure 9a). Rather, the kinetic energy keeps an approximately constant value without decay, and meanwhile the magnetic energy decreases slowly. Moreover, no matter at which moment the boundary driving is switched off, the system will always reach an eruption phase after a short interval of evolution (for instance, see the case with sunspot rotation stopped at $t = 23\ t_s$, for which the magnetic field and current density evolution are shown in the animation attached for Figure 9). These experiments show that the bottom driving is not necessary in maintaining the slow rise phase (once it begins), although it can slightly speed up this process. The time duration of slow rise phase is around 8 t_s, which is on the same order of that of the observed slow rise phase (around 20 min).

Why the slow rise phase must proceed for a short interval before the eruption, regardless of the bottom boundary driving? This is because only when the current sheet reaches the critical thickness can the eruption be triggered by reconnection. In Figure 9b, we also show evolution of the thickness of the current sheet in the different runs. As can be seen, the current layer is continually thinned and once its thickness is below the resolvable limit of the grid resolution (about 3 grid sizes), the impulsive acceleration of the fast eruption phase begins. When turning off the bottom driving at $t = 23\ t_s$, the current layer is still thinned although the rate is slightly slower, and the eruption is initiated in the same way when the current sheet reaches the critical thickness. In contrast, when the boundary driving is stopped at $t = 20\ t_s$ before the slow-rise phase begins, the system will relax to an equilibrium without changing the thickness of the current layer, and thus cannot develop the current sheet as required for reconnection.

Although our simulations suggest a slow rise phase analogous to the observed one, the duration of this phase should be sensitive to the magnitudes of the resistivity and the bottom boundary driving. If the resistivity is smaller, the eruption is expected to be delayed since a thinner current sheet would form and needs more time, thus this phase would be longer. With a slower driving speed at the bottom boundary, this phase is also expected to be longer. In our simulations, both the resistivity and the driving speed are much larger than the real values, for which it is formidable to realize at present in numerical simulations.

5. CONCLUSIONS AND DISCUSSION

In this paper, based on observation and MHD simulations, we have studied the process of a rotating sunspot in AR NOAA 12158 causing a major solar eruption. Our simulations demonstrated that the continuous rotation of a major sunspot of the AR leads to an eruption in a way distinct from the conventional view based on ideal MHD instabilities of twisted flux rope. It is found that through the successive rotation of the sunspot the coronal field is sheared with a vertical current sheet created progressively, and once fast reconnection sets in at the current sheet, the eruption is instantly triggered, and a highly twisted flux rope originates from the eruption, forming a CME. The simulations also revealed explicitly a slow-rise evolution phase between the quasi-static phase of non-potential magnetic energy storage and the impulsive acceleration phase of eruption. Such a slow-rise phase is commonly observed in many eruption events (including the studied one) for either erupting filaments or coronal loops but still lacks a physical explanation. Our analysis suggests that the slow-rise phase is inherent to the coronal dynamics when close to eruption rather than controlled by the photospheric driving motions as considered before (Vršnak 2019). Once it begins the slow-rise phase develops for a short time interval (often with a few tens of minutes), even if the boundary driving is turned off, and eventually transforms into an eruption. This short phase plays an important role in building up of the current sheet, since it accelerates the thinning of the current layer that is built up in the quasi-static phase until the reconnection sets in.

Why do our simulations support such a scenario rather than that based on MHD instabilities of pre-eruption MFRs? There are two reasons. Firstly, the rotation of sunspot is too slow to form a well-defined MFR in a few days. Observations show that the angular rotational speed for many sunspots is on average a few degrees per hour and the total rotation degree is mostly between 40–200° over periods of

3–5 days (Brown et al. 2003). Thus, the resulted magnetic twist by such rotation is far lower than that necessary to form a well-defined MFR (which needs field lines winding around an axis with at least one turn, or twist of 360°) and further to trigger the ideal kink instability (which needs winding number of more than 1.25 turns (Hood & Priest 1979) or twist of more than 450°). Even though the sunspot in the well known AR 10930 is reported to rotate by a very large amount of about 500° over five days (Min & Chae 2009), there were many eruptions in that duration (AR 10930 produced 4 homologous X-class eruptive flares and a few smaller ones) and thus these eruptions should release substantially the built-up twist repeatedly, preventing the continuous formation of a well-defined twisted rope. Indeed, this is supported by a previous study of AR 10930 (Wang et al. 2022), in which a MHD simulation was carried out using a similar approach in this paper. In that work, the simulation started with a potential magnetic field reconstructed from the observed magnetogram and then rotational motion is applied to the positive sunspot of the AR to mimic the observed rotation. That simulation successfully showed that the sunspot rotation produced homologous eruptions having reasonable consistency with observations in relative strength, energy release, spatial features (such as pre-eruption sigmoid and flare ribbons), and time intervals of eruptions. In addition, in the simulation the total angle of rotation of the sunspot until the eruption onset is also very close to the observed value. The key finding is also similar to this paper: as driven by the sunspot rotation, current sheet is formed above the main PIL between the two major magnetic polarities of the AR, and the eruptions are triggered by fast reconnection in the pre-eruption formed current sheet.

Secondly, sunspot rotation, although slow, is a very efficient way of injecting magnetic free energy. For example, by modelling of a solar flare from 13 May 2005, it has been shown that the sunspot rotation of the source AR dominates the energy accumulation for the flare event (Kazachenko et al. 2009). In fact, such sunspot rotation alone can store sufficient energy to power a very large flare. Our simulation demonstrated this point more clearly as shown in Figure 9a; by a rotation of 90° (on average for the whole sunspot), the free energy has been increased by over 50% of the potential field energy. As the open field energy is an upper limiter, which is around 2.5 times of the potential field energy, this made it very easy for the field to reach the open field energy, if the rotation is as large as 300°. The open field is closely related to the building up of the current sheet, since a current sheet must be built up before the field becoming fully open, as consistent with our previous high-resolution simulation based on a simple bipolar field (Jiang et al. 2021c). Thus, to build up a current sheet needs much less degree of rotation than that for building up an unstable MFR, as the former is more consistent with the observation of the rotation degrees.

Nevertheless, there is also a possibility in some events that the rotation of sunspot drives the formation of the current sheet, but a confined flare is resulted if the overlying field is strong enough (or decay slowly enough) to constrain the newly-formed, erupting flux rope. With continuous rotation, such confined flares might occur multiple times and jointly build up an ideal unstable MFR that eventually erupts, as suggested by recent observations (James et al. 2020). Another possibility is that during the sunspot rotation, continuous slow reconnection might occur at near the photosphere, which is often associated with the observed flux cancellation, can also help to build up unstable MFR before eruption. This will need further investigations with data-driven MHD simulations (Jiang et al. 2022).

ACKNOWLEDGMENTS

This work is jointly supported by Shenzhen Science and Technology Program (Grant No. RCJC20210609104422048), Shenzhen Technology Project JCYJ20190806142609035, Shenzhen Key Laboratory Launching Project (No. ZDSYS20210702140800001), Guangdong Basic and Applied Basic Research Foundation (2023B1515040021) and National Natural Science Foundation of China (NSFC 42174200). Data from observations are courtesy of NASA SDO/AIA and the HMI science teams. The computational work was carried out on TianHe-1(A), National Supercomputer Center in Tianjin, China.

REFERENCES

Aly, J. J. 1991, The Astrophysical Journal, 375, L61, doi: 10.1086/186088

Amari, T., Luciani, J. F., Aly, J. J., Mikic, Z., & Linker, J. 2003, The Astrophysical Journal, 595, 1231, doi: 10.1086/377444

Amari, T., Luciani, J. F., Aly, J. J., & Tagger, M. 1996, The Astrophysical Journal, 466, L39, doi: 10.1086/310158

Aschwanden, M. J. 2019, Astrophysics and Space Science Library, Vol. 458, New Millennium Solar Physics (Cham: Springer International Publishing), doi: 10.1007/978-3-030-13956-8

Aulanier, G., Démoulin, P., & Grappin, R. 2005, Astronomy & Astrophysics, 430, 1067, doi: 10.1051/0004-6361:20041519

Aulanier, G., Török, T., Démoulin, P., & DeLuca, E. E. 2010, The Astrophysical Journal, 708, 314, doi: 10.1088/0004-637X/708/1/314

Barnes, C. W., & Sturrock, P. A. 1972, The Astrophysical Journal, 174, 659, doi: 10.1086/151527
Bhattacharjee, A., Huang, Y.-M., Yang, H., & Rogers, B. 2009, Physics of Plasmas, 16, 112102, doi: 10.1063/1.3264103
Bi, Y., Jiang, Y., Yang, J., et al. 2016, Nature Communications, 7, 13798, doi: 10.1038/ncomms13798
Bian, X., Jiang, C., Feng, X., Zuo, P., & Wang, Y. 2022a, The Astrophysical Journal Letters, 925, L7, doi: 10.3847/2041-8213/ac4980
Bian, X., Jiang, C., Feng, X., et al. 2022b, Astronomy & Astrophysics, 658, A174, doi: 10.1051/0004-6361/202141996
Brown, D., Nightingale, R., Alexander, D., et al. 2003, Solar Physics, 216, 79, doi: 10.1023/A:1026138413791
Brown, D., & Walker, A. 2021, Solar Physics, 296, 48, doi: 10.1007/s11207-021-01787-4
Chen, J. 2017, Physics of Plasmas, 24, 090501, doi: 10.1063/1.4993929
Cheng, X., Guo, Y., & Ding, M. 2017, Science China Earth Sciences, 60, 1383, doi: 10.1007/s11430-017-9074-6
Cheung, M. C. M., & DeRosa, M. L. 2012, The Astrophysical Journal, 757, 147, doi: 10.1088/0004-637X/757/2/147
Daughton, W., Roytershteyn, V., Karimabadi, H., et al. 2011, Nature Physics, 7, 539, doi: 10.1038/nphys1965
Démoulin, P., Priest, E. R., & Lonie, D. P. 1996, Journal of Geophysical Research: Space Physics, 101, 7631, doi: 10.1029/95JA03558
Duan, A., Jiang, C., Hu, Q., et al. 2017, The Astrophysical Journal, 842, 119, doi: 10.3847/1538-4357/aa76e1
Dudík, J., Polito, V., Janvier, M., et al. 2016, The Astrophysical Journal, 823, 41, doi: 10.3847/0004-637X/823/1/41
Emslie, A. G., Dennis, B. R., Shih, A. Y., et al. 2012, The Astrophysical Journal, 759, 71, doi: 10.1088/0004-637X/759/1/71
Evershed., J. 1910, Monthly Notices of the Royal Astronomical Society, 70, 217, doi: 10.1093/mnras/70.3.217
Fan, Y., & Gibson, S. E. 2007, The Astrophysical Journal, 668, 1232, doi: 10.1086/521335
Feng, X., Zhou, Y., & Wu, S. T. 2007, The Astrophysical Journal, 655, 1110, doi: 10.1086/510121
Forbes, T. G., & Isenberg, P. A. 1991, The Astrophysical Journal, 373, 294, doi: 10.1086/170051
Galsgaard, K., & Nordlund, Å. 1997, Journal of Geophysical Research: Space Physics, 102, 219, doi: 10.1029/96JA01462
Gou, T., Liu, R., Veronig, A. M., et al. 2023, Nature Astronomy, doi: 10.1038/s41550-023-01966-2
Green, L. M., Török, T., Vršnak, B., Manchester, W., & Veronig, A. 2018, Space Science Reviews, 214, 46, doi: 10.1007/s11214-017-0462-5
Harvey, K., & Harvey, J. 1973, Solar Physics, 28, 61, doi: 10.1007/BF00152912
He, W., Hu, Q., Jiang, C., Qiu, J., & Prasad, A. 2022, The Astrophysical Journal, 934, 103, doi: 10.3847/1538-4357/ac78df
Hood, A. W., & Priest, E. R. 1979, Solar Physics, 64, 303, doi: 10.1007/BF00151441
James, A. W., Green, L. M., van Driel-Gesztelyi, L., & Valori, G. 2020, Astronomy & Astrophysics, doi: 10.1051/0004-6361/202038781
Jiang, C., Bian, X., Sun, T., & Feng, X. 2021a, Frontiers in Physics, 9, 646750, doi: 10.3389/fphy.2021.646750
Jiang, C., Chen, J., Duan, A., et al. 2021b, Frontiers in Physics, 9, 746576, doi: 10.3389/fphy.2021.746576
Jiang, C., & Feng, X. 2014, Solar Physics, 289, 63, doi: 10.1007/s11207-013-0346-0
Jiang, C., Feng, X., Guo, Y., & Hu, Q. 2022, The Innovation, 3, 100236, doi: 10.1016/j.xinn.2022.100236
Jiang, C., Feng, X., Zhang, J., & Zhong, D. 2010, Solar Physics, 267, 463, doi: 10.1007/s11207-010-9649-6
Jiang, C., & Toriumi, S. 2020, The Astrophysical Journal, 903, 11, doi: 10.3847/1538-4357/abb5ac
Jiang, C., Wu, S. T., Feng, X., & Hu, Q. 2016, NATURE COMMUNICATIONS, 11
Jiang, C., Feng, X., Liu, R., et al. 2021c, Nature Astronomy, 5, 1126, doi: 10.1038/s41550-021-01414-z
Jiang, Y., Zheng, R., Yang, J., et al. 2012, The Astrophysical Journal, 744, 50, doi: 10.1088/0004-637X/744/1/50
Kazachenko, M. D., Canfield, R. C., Longcope, D. W., et al. 2009, The Astrophysical Journal, 704, 1146, doi: 10.1088/0004-637X/704/2/1146
Kilpua, E. K. J., Pomoell, J., Price, D., Sarkar, R., & Asvestari, E. 2021, Frontiers in Astronomy and Space Sciences, 8, 631582, doi: 10.3389/fspas.2021.631582
Kliem, B., Lin, J., Forbes, T. G., Priest, E. R., & Török, T. 2014, The Astrophysical Journal, 789, 46, doi: 10.1088/0004-637X/789/1/46
Kliem, B., & Török, T. 2006, Physical Review Letters, 96, 255002, doi: 10.1103/PhysRevLett.96.255002
Li, T., & Zhang, J. 2015, The Astrophysical Journal, 804, L8, doi: 10.1088/2041-8205/804/1/L8
Lin, J., & Forbes, T. G. 2000, Journal of Geophysical Research: Space Physics, 105, 2375, doi: 10.1029/1999JA900477
Liu, C., Deng, N., Lee, J., et al. 2014, The Astrophysical Journal, 795, 128, doi: 10.1088/0004-637X/795/2/128
Liu, R. 2020, Research in Astronomy and Astrophysics, 20, 165, doi: 10.1088/1674-4527/20/10/165
Liu, R., Kliem, B., Titov, V. S., et al. 2016, The Astrophysical Journal, 818, 148, doi: 10.3847/0004-637X/818/2/148
Liu, Y., & Schuck, P. W. 2012, The Astrophysical Journal, 761, 105, doi: 10.1088/0004-637X/761/2/105
Mikic, Z., Schnack, D. D., & van Hoven, G. 1990, The Astrophysical Journal, 361, 690, doi: 10.1086/169232

Min, S., & Chae, J. 2009, Solar Physics, 258, 203, doi: 10.1007/s11207-009-9425-7

Moore, R. L., Sterling, A. C., Hudson, H. S., & Lemen, J. R. 2001, The Astrophysical Journal, 552, 833, doi: 10.1086/320559

Schuck, P. W. 2008, The Astrophysical Journal, 683, 1134, doi: 10.1086/589434

Shen, J., Ji, H., & Su, Y. 2022, Research in Astronomy and Astrophysics, 22, 015019, doi: 10.1088/1674-4527/ac389b

St. John, C. E. 1913, The Astrophysical Journal, 37, 322, doi: 10.1086/142002

Stenflo, J. O. 1969, Solar Physics, 8, 115, doi: 10.1007/BF00150662

Sturrock, P. A. 1991, The Astrophysical Journal, 380, 655, doi: 10.1086/170620

Titov, V. S., Hornig, G., & Démoulin, P. 2002, Journal of Geophysical Research: Space Physics, 107, SSH 3, doi: 10.1029/2001JA000278

Török, T., & Kliem, B. 2003, Astronomy & Astrophysics, 406, 1043, doi: 10.1051/0004-6361:20030692

—. 2005, The Astrophysical Journal, 630, L97, doi: 10.1086/462412

Török, T., Temmer, M., Valori, G., et al. 2013, Solar Physics, 286, 453, doi: 10.1007/s11207-013-0269-9

Vemareddy, P., Ambastha, A., & Maurya, R. A. 2012, The Astrophysical Journal, 761, 60, doi: 10.1088/0004-637X/761/1/60

Vemareddy, P., Cheng, X., & Ravindra, B. 2016, The Astrophysical Journal, 829, 24, doi: 10.3847/0004-637X/829/1/24

Vršnak, B. 2008, Annales Geophysicae, 26, 3089, doi: 10.5194/angeo-26-3089-2008

—. 2019, Frontiers in Astronomy and Space Sciences, 6, 28, doi: 10.3389/fspas.2019.00028

Wang, X., Jiang, C., Feng, X., Duan, A., & Bian, X. 2022, The Astrophysical Journal, 938, 61, doi: 10.3847/1538-4357/ac8d0e

Wiegelmann, T., Inhester, B., & Sakurai, T. 2006, Solar Physics, 233, 215, doi: 10.1007/s11207-006-2092-z

Yamamoto, T. T., & Kusano, K. 2012, The Astrophysical Journal, 752, 126, doi: 10.1088/0004-637X/752/2/126

Yan, X.-L., Qu, Z.-Q., & Kong, D.-F. 2008, Monthly Notices of the Royal Astronomical Society, 391, 1887, doi: 10.1111/j.1365-2966.2008.14002.x

Yan, X. L., Wang, J. C., Pan, G. M., et al. 2018a, The Astrophysical Journal, 856, 79, doi: 10.3847/1538-4357/aab153

Yan, X. L., Yang, L. H., Xue, Z. K., et al. 2018b, The Astrophysical Journal, 853, L18, doi: 10.3847/2041-8213/aaa6c2

Zhang, J., Li, L., & Song, Q. 2007, The Astrophysical Journal, 662, L35, doi: 10.1086/519280

Zheng, J., Yang, Z., Guo, J., et al. 2017, Research in Astronomy and Astrophysics, 17, 081, doi: 10.1088/1674-4527/17/8/81